AGU ADVANCING EARTH AND SPACE SCIENCE

Geophysical Research Letters®

RESEARCH LETTER
10.1029/2021GL093923

Key Points:

- Subglacial freshwater discharge substantially enhances ice shelf melting locally in ocean simulations
- Subglacial freshwater discharge allows to reproduce complex patterns of ice shelf melt with high melt close to the grounding line
- Meltwater follows topographically constrained current and spreads into mid-depths at the ice shelf front

Supporting Information:

Supporting Information may be found in the online version of this article.

Correspondence to:

Y. Nakayama,
Yoshihiro.Nakayama@lowtem.hokudai.ac.jp

Citation:

Nakayama, Y., Cai, C., & Seroussi, H. (2021). Impact of subglacial freshwater discharge on Pine Island ice shelf. *Geophysical Research Letters*, *48*, e2021GL093923. https://doi.org/10.1029/2021GL093923

Received 30 APR 2021
Accepted 1 SEP 2021

Impact of Subglacial Freshwater Discharge on Pine Island Ice Shelf

Yoshihiro Nakayama[1], Cilan Cai[2], and Helene Seroussi[3]

[1]Institute of Low Temperature Science, Hokkaido University, Sapporo, Japan, [2]The Department of Earth System Science, Tsinghua University, Beijing, China, [3]Thayer School of Engineering, Dartmouth College, Hanover, NH, USA

Abstract Satellite-based estimates of ice shelf melt rates reach ~200 m yr^{-1} close to the grounding line of Pine Island Glacier, in West Antarctica. However, ocean simulations have not yet been able to reproduce such high melt rates, even with high-resolution models. Here, we use a regional model of Pine Island ice shelf cavity and study the impact of subglacial freshwater discharge on simulated ice shelf melt rates and ocean circulation in the cavity. We show that subglacial freshwater discharge substantially enhances ice shelf melting close to the grounding line, successfully simulating high ice shelf melt rates suggested by observations. The buoyant mixture of glacial meltwater plume rises to ~27.4 isopycnal surfaces, following topographically constrained current, and spreads into mid-depths at the ice shelf front. The role of freshwater discharge is likely to remain unchanged over the coming decades given the projected evolution of runoff and rainfall over Pine Island basin.

Plain Language Summary Pine Island Glacier is located in the Amundsen Sea Embayment, a region experiencing large amounts of melting, thinning, and acceleration. Melt rates close to the grounding line, in particular, reach very high values and have a significant impact on the future evolution of glaciers and their contributions to sea-level rise. However, they are poorly captured by current numerical ocean models. In this study, we use a regional model of Pine Island ice shelf cavity and study the impact of subglacial freshwater discharge exiting at the base of the glacier, at its grounding line, on simulated melt rates and ocean circulation in the ice shelf cavity. We show that subglacial freshwater discharge substantially enhances the ice shelf melting close to the grounding line, successfully simulating high ice shelf melt rates suggested by observations. The buoyant mixture of glacial meltwater plume rises to the shallower depths following topographically constrained current and spreads into mid-depths at the ice shelf front. The limited evolution of runoff and rainfall projected over Pine Island Glacier suggests the role of subglacial freshwater discharge will likely remain similar over the coming decades.

1. Introduction

Pine Island Glacier, in the Amundsen Sea sector of West Antarctica, experienced large grounding line retreat, thinning, and acceleration over the past four decades (Depoorter et al., 2013; Mouginot et al., 2014; Paolo et al., 2015; Rignot et al., 2013, 2019; Shepherd et al., 2012, 2018), contributing the equivalent of 3.0 mm of global sea-level rise between 1979 and 2017 (Rignot et al., 2019). These changes were triggered by increasing amounts of sub-ice shelf melt under Pine Island ice shelf (PIIS), caused by intrusions of warm modified Circumpolar Deep Water (mCDW, about 3°C warmer than the in situ freezing point) that is transported onto the continental shelf through submarine glacial troughs (Dutrieux et al., 2014; Jacobs et al., 2011; Nakayama et al., 2013; Pritchard et al., 2012). Satellite-based estimates of ice shelf melt rate close to the grounding line of Pine Island reach ~200 m yr^{-1} locally (Shean et al., 2019) and the rapid melting close to the grounding line impacts its grounding line evolution as well as its future contribution to sea-level rise (Cornford et al., 2015; Favier et al., 2014; Joughin et al., 2014; Nias et al., 2016; Seroussi, Nakayama, et al., 2017).

Ocean simulations of ice shelf melt rates are, however, not yet able to reproduce such high melt rates (Jourdain et al., 2019; Nakayama et al., 2019; Schodlok et al., 2015; Seroussi, Nakayama, et al., 2017), as they face several challenges: (a) a fine-scale grid resolution is required to accurately resolve the ice shelf cavity geometry, (b) coupled ice-ocean models that capture the feedback between these two components are only starting to emerge, and (c) limited in situ observations are available in ice shelf cavities, especially close

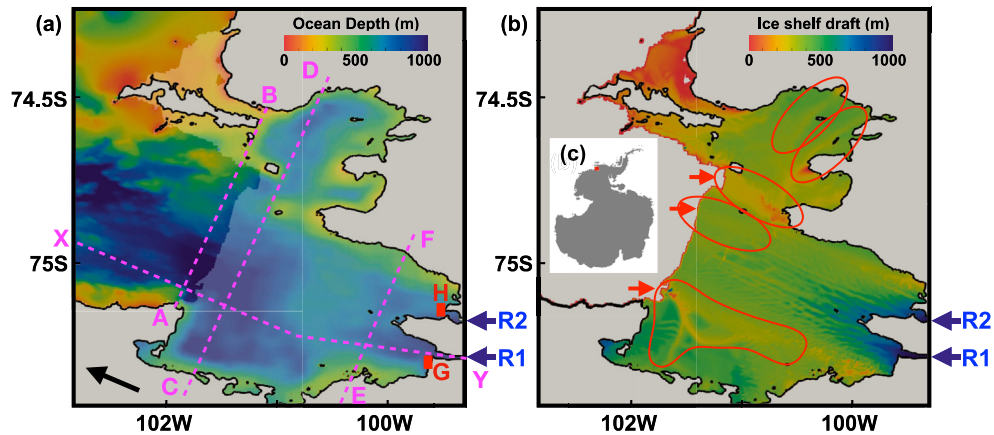

Figure 1. (a) Ocean bathymetry with partially transparent white patch indicating Pine Island ice shelf location. R1 and R2 show subglacial freshwater flux outlets on the eastern model boundary in the Qsg experiments and G and H indicate the locations used for the spatial averages of ice shelf melt rate, thermal driving, and ocean current. Pink dashed lines show the locations of vertical sections used in Figures 2, 4 and S3. Black arrow indicates the Ice flow direction. (b) Pine Island ice shelf draft. Red arrows and regions enclosed by red lines indicate sub-ice shelf channels. (c) Antarctic map with the red box denoting the model domain.

to the grounding line. Nakayama et al. (2019) have developed an ocean simulation at an unprecedentedly high-resolution (~200 m horizontal and 10 m vertical resolutions) that resolves shelf-sea and sub-ice-shelf environments for the eastern Amundsen Sea. Results highlight a good agreement with observations overall but are unable to reproduce the high melt rate estimates close to the grounding lines of Pine Island and Thwaites glaciers (Milillo et al., 2019; Shean et al., 2019): modeled PIIS melt rates reach ~80 m yr^{-1}, which is ~2.5 time smaller than the ~200 m yr^{-1} remote-sensing estimates of melt rate in the area (Milillo et al., 2019; Shean et al., 2019). In Greenland, studies have shown that an increase in subglacial freshwater discharge at the grounding line leads to a higher rate of melting along the ice front and under floating ice shelves (Cai et al., 2017; Cowton et al., 2018; Morlighem et al., 2019; Sciascia et al., 2014; Slater et al., 2018; Straneo et al., 2011; Xu et al., 2012, 2013). For Antarctic ice shelves, the importance of subglacial freshwater discharge is only starting to be discussed (Wei et al., 2020).

We use a regional ocean simulation of the PIIS cavity to investigate (a) the impact of subglacial freshwater discharge on ice shelf basal melt and (b) pathways of glacial meltwater in the ice shelf cavity. The simulations are based on the high-resolution configuration of Nakayama et al. (2019) and include subglacial freshwater discharge following Cai et al. (2017).

2. Methods and Experiments

2.1. Ocean Model

We use a regional configuration of the Massachusetts Institute of Technology general circulation model with hydrostatic approximation, dynamic/thermodynamic sea-ice (Losch et al., 2010), and thermodynamic ice shelf (Losch, 2008). Nominal horizontal and vertical grid resolutions are ~200 and 10 m, respectively. We compute ice shelf melt rates from a three-equation model (Hellmer & Olbers, 1989; Holland & Jenkins, 1999; Jenkins, 1991) using velocity-dependent exchange of heat and salt at the ice shelf base. This model is almost identical to Nakayama et al. (2019), the only differences being: (a) the model domain only includes the PIIS cavity (Figure 1), (b) the ocean bathymetry and ice shelf draft are based on the updated BedMachine-Antarctica (Morlighem et al., 2020), and (c) the lateral ocean boundary conditions are provided by the latest version of Nakayama et al. (2019) with improved representations of mCDW properties. A passive tracer is released at the ice shelf base at the same rate as melting occurs to track glacial meltwater (Nakayama et al., 2017). Tidal impact is small for the PIIS so tides are not included (Nakayama et al., 2019).

2.2. Experiments

We conduct five experiments with varying amounts of subglacial freshwater discharge, that all start from the same conditions on January 30, 2010 (defined as day 0), after a 30-day spin-up with no subglacial freshwater discharge. The control (CTRL) experiment has no subglacial freshwater discharge. All five sensitivity experiments include subglacial freshwater discharge in two locations at the easter model boundary, denoted R1 and R2 in Figure 1, that coincide with the grounding line. All experiments end on February 28, 2010 (day 29). Freshwater discharges are applied over areas of 200 m by 20 m with fluxes of 0.011 m s^{-1} and 0.0036 m s^{-1} for the Qsg experiment, respectively, for R1 and R2.

The water amount is estimated using a steady-state thermal model based on an enthalpy formulation (Aschwanden et al., 2012) implemented and tested in the Ice-sheet and Sea-Level System Model (Kleiner et al., 2015; Seroussi et al., 2013). Surface velocities (Rignot et al., 2011) are reproduced using data assimilation to constrain basal friction (Morlighem et al., 2010). The geothermal flux is from Shapiro and Ritzwoller (2004), the surface temperature from RACMO2.1 (Lenaerts et al., 2012), and the general procedure to run the thermal model is similar to Seroussi, Ivins, et al. (2017). The water produced at the ice base is then routed under the ice using the routing model from the TopoToolbox (Schwanghart & Scherler, 2014) and the geometry from BedMachine-Antarctica (Morlighem et al., 2020). We only consider the two main locations of water discharge in PIIS cavity at R1 and R2. Three other locations display water discharge in PIIS cavity, but the amount of water discharge in these locations is an order of magnitude smaller than the R2 discharge and are therefore not included in our simulations. The subglacial discharge used in the Qsg experiment (1.3 and 0.41 Gt yr^{-1} at R1 and R2 discharge locations, respectively) represents a time average melt caused by geothermal heat flux and frictional heat at the base of the grounded ice, similar to Joughin et al. (2009). Three additional experiments with 2, 10, and 50 times more freshwater (2*Qsg, 10*Qsg, and 50*Qsg, respectively) compared to the Qsg case are also performed (Table S1).

Ocean conditions under the PIIS cavity show little temporal variations over the simulation period, especially close to the grounding line (Nakayama et al., 2019). Thus, we mainly analyze average properties over the last 10 days (day 20–29).

3. Results

The regional simulation of the eastern Amundsen Sea (Nakayama et al., 2019) has been extensively compared with existing observations (Davis et al., 2018; Dutrieux et al., 2014; Jacobs & Giulivi, 2010; Jenkins et al., 2010; Nakayama et al., 2013; Webber et al., 2017). We refer interested readers to Nakayama et al. (2019) for more details.

3.1. Control Simulation

The CTRL experiment simulates the ocean conditions in the absence of subglacial freshwater discharge. The last 10-day mean potential temperature, salinity, and glacial meltwater fraction along a vertical section going from open water to the PIIS grounding line (vertical section X-Y in Figure 1a) show the inflow of mCDW into the cavity (Figures 2a and 2b), similar to observations (Jenkins et al., 2010; Nakayama et al., 2019). The ice shelf melt rates close to the grounding line in boxes G and H reach ~80 m yr^{-1} and ~ 40 m yr^{-1}, respectively (Figures 3a and 3d, and Table S2).

The mixture of mCDW and glacial meltwater is buoyant compared to surrounding water masses, and rises toward the lighter isopycnal surfaces. The glacial meltwater fraction is ~0.5% close to the grounding line (see red arrow in Figure 2c) and increases toward the shallower depth (at 300–450 m depths) as the ice shelf continues to melt in the middle to the outer part of ice shelf away from the grounding line. The ice shelf meltwater fraction reaches ~1.5% in the outer part of the ice shelf cavity at depths of 300–450 m (Figure 2c). This maximum is located over the ~27.4 isopycnals, while almost no glacial meltwater can be identified below the 27.6 isopycnal. Glacial meltwater is concentrated at depths of 200–400 m close to the ice front (Figures 2c and 4g), consistent with the observations of glacial meltwater fraction at the ice shelf front (Biddle et al., 2019; Dutrieux et al., 2014; Garabato et al., 2017; Jacobs et al., 2011; Nakayama et al., 2013).

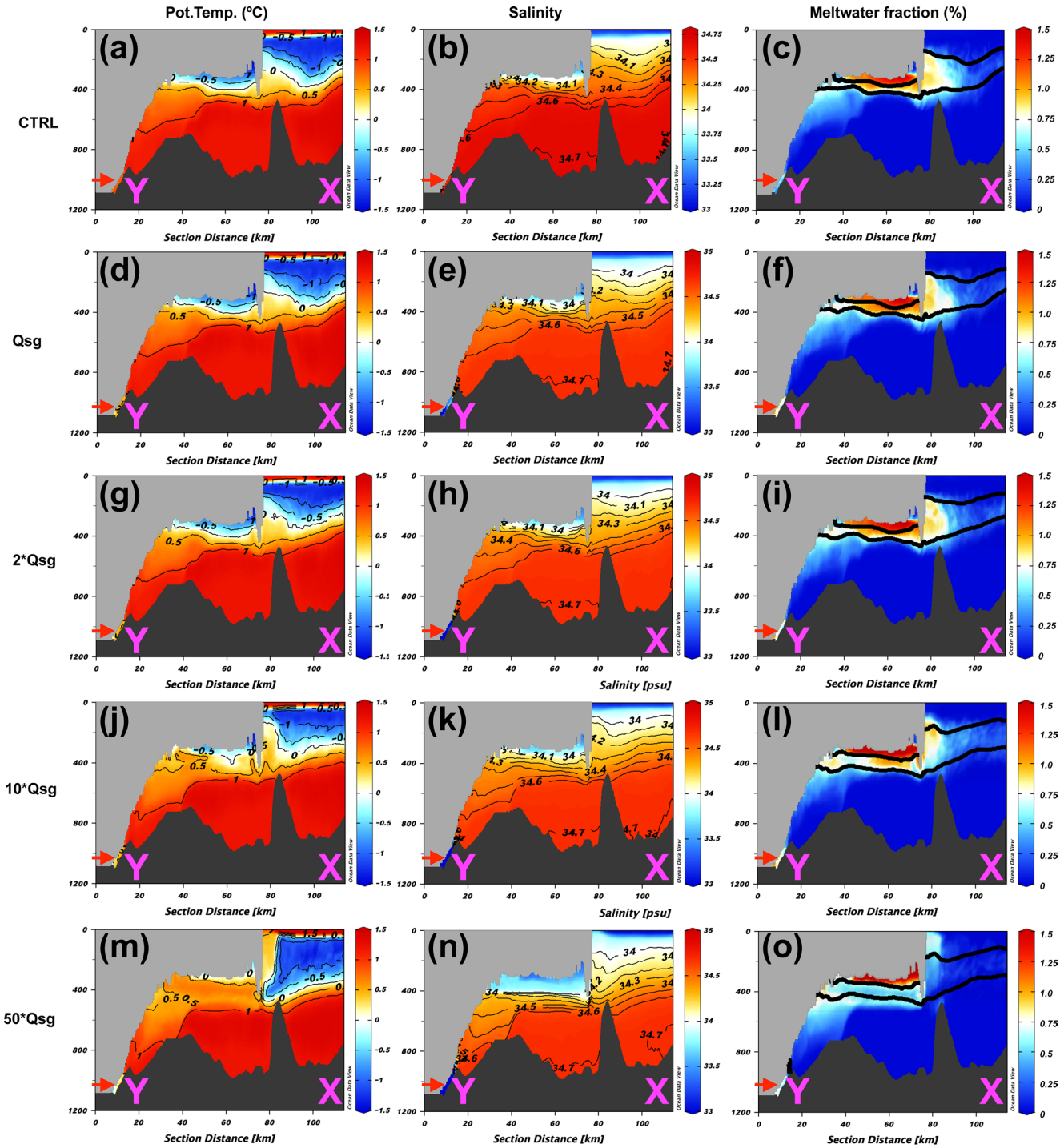

Figure 2. Ten-day average (day 20–29) potential temperature (a, d, g, j, m), salinity (b, e, h, k, n), and glacial meltwater fraction (c, f, i, l, o) along section X-Y for the control (CTRL) (a–c), Qsg (d–f), 2*Qsg (g–i), 10*Qsg (j–l), and 50*Qsg (m–o) experiments, respectively. Thick black lines on the panels (c, f, i, l, and o), show the 27.4 kg m^{-3} and 27.6 kg m^{-3} isopycnals. Red arrows indicate the region close to the grounding line.

The horizontal distributions of glacial meltwater along the 27.4 and 27.6 isopycnal surfaces (Figure 3) show the pathways of glacial meltwater toward the open ocean. Water with high meltwater fraction (~1.5%) can be identified in the ice shelf channels on the 27.4 isopycnal (Figure 3g). Some of these channels extend along the flow direction of PIIS (red arrows and region enclosed by red lines in Figure 1b). On the 27.6-isopycnal, glacial meltwater fraction is smaller with peak values of ~1%. The spatial pattern presents rather

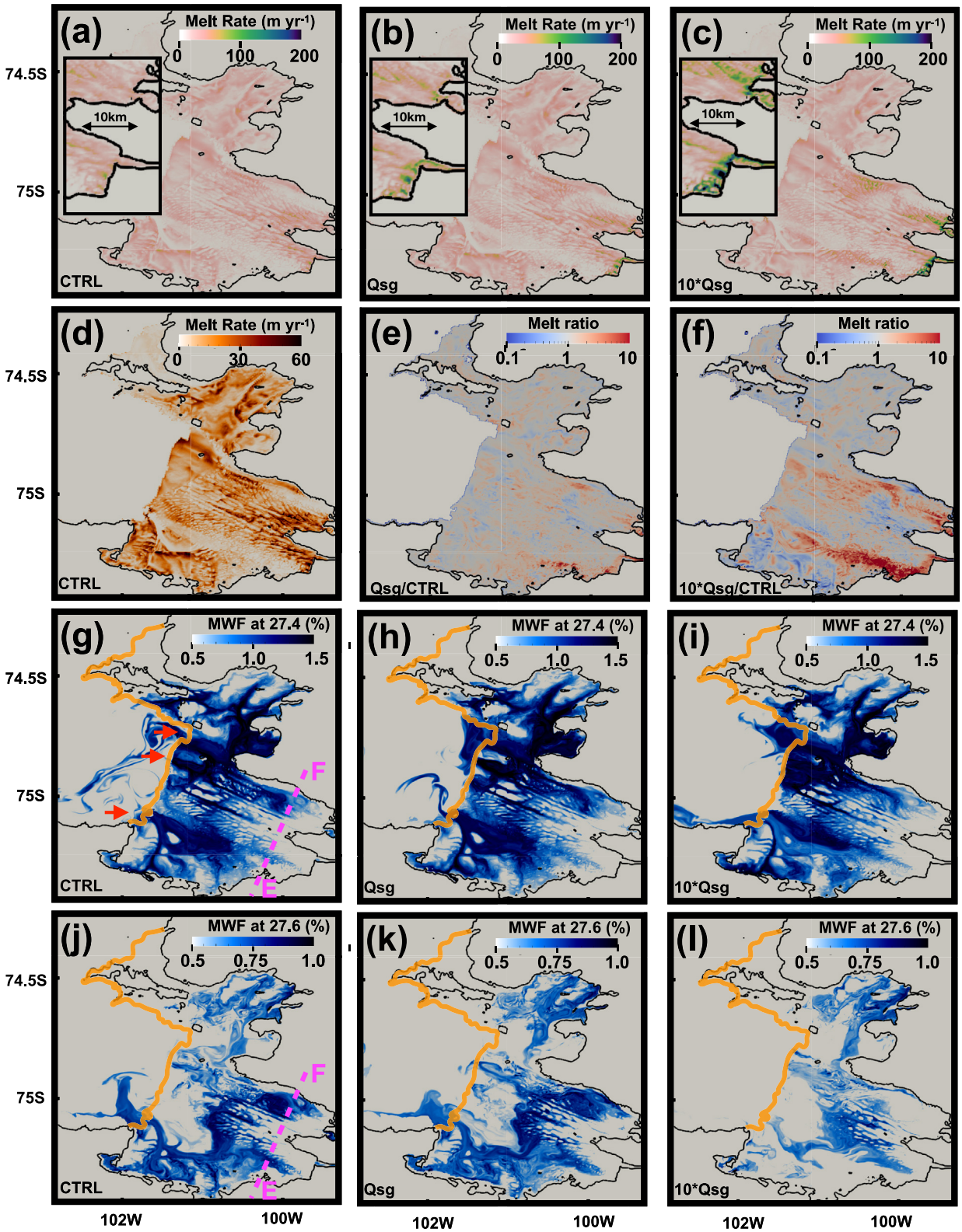
(a)
Melt Rate (m yr-1)
0 100 200
10km
CTRL
(b)
Melt Rate (m yr-1)
0 100 200
10km
Qsg
(c)
Melt Rate (m yr-1)
0 100 200
10km
10*Qsg
(d)
Melt Rate (m yr-1)
0 30 60
CTRL
(e)
Melt ratio
0.1 1 10
Qsg/CTRL
(f)
Melt ratio
0.1 1 10
10*Qsg/CTRL
(g)
MWF at 27.4 (%)
0.5 1.0 1.5
F
E
CTRL
(h)
MWF at 27.4 (%)
0.5 1.0 1.5
Qsg
(i)
MWF at 27.4 (%)
0.5 1.0 1.5
10*Qsg
(j)
MWF at 27.6 (%)
0.5 0.75 1.0
F
E
CTRL
(k)
MWF at 27.6 (%)
0.5 0.75 1.0
Qsg
(l)
MWF at 27.6 (%)
0.5 0.75 1.0
10*Qsg
74.5S
75S
102W
100W

Figure 3.

different pathways of glacial melt-mCDW mixture toward the ice shelf front (Figure 3j), likely influenced by cavity scale circulation.

The vertical sections A-B, C-D, and E-F are somewhat perpendicular to the ice flow direction of Pine Island Glacier (black arrow in Figure 1) and show the vertical structures of glacial meltwater outflow at different locations in the cavity. We observe two local maxima of glacial meltwater close to the grounding line along section E-F (see red arrows in Figure 4i). These two peaks are formed because of the high ice shelf melt rate in these areas (see Figure 3d), corresponding to R1 and R2 in Figure 1. A thick portion of the ice shelf with a deep draft between them prevents glacial meltwater from merging into one channel (Figure 4i). Consistent with Nakayama et al. (2019), topographically constrained boundary currents are found transporting mCDW toward the grounding line. East-southeastward current (toward the grounding line) is found over the northward-shallowing slopes (magenta arrows in Figure 4l), while west-northwestward current (toward the ice shelf front) is found over the northward-deepening slopes (cyan arrows in Figure 4l) of the two small-scale troughs.

Section C-D, located ~70 km downstream, shows a clear two-layer structure. The thermocline is located at ~400-m depth, separating mCDW from the upper colder and fresher Winter Water (Figures 4b and 4e). Glacial meltwater is concentrated above the thermocline (Figure 4h). Although the velocity structure is more complex than for section E-F, east-southeastward currents are predominantly found over the northward-shallowing slopes (the magenta arrows in Figure 4k), while west-northwestward currents are found over the northward-deepening slopes, similar to section E-F. This topographically constrained current plays an important role in determining the pathways of ice shelf meltwater.

Section A-B, located just outside of the cavity, shows two peaks of glacial meltwater fraction concentrated between 200 and 400 m on both sides of the section. The locations of glacial meltwater outflows are over the northward-deepening slopes (cyan arrows in Figure 4j) similar to section C-D.

3.2. Impact of Subglacial Freshwater Discharge

We conduct four sensitivity experiments showing transient responses to varying amounts of subglacial freshwater discharges (Table S1). Time series of PIIS cavity's total kinematic energy for Qsg and 2*Qsg remain similar compared to CTRL (Figure S1). These results indicate that Qsg and 2*Qsg cases reach quasi-steady state during the sensitivity experiments. For all sensitivity experiments, ice shelf basal melt rates stabilize within 15 days (Figure S1). The total PIIS melt rates are 58.3 Gt yr^{-1}, 61.6 Gt yr^{-1}, 63.2 Gt yr^{-1}, 69.2 Gt yr^{-1}, and 85.4 Gt yr^{-1} for CTRL, Qsg, 2*Qsg, 10*Qsg, and 50*Qsg, respectively (Table S2). The overall spatial distributions of ice-shelf melt rate are similar in all experiments (Figures 3 and S2), with patterns of melt rates correlating with the channels at the base of the ice shelf and largest melt rates close to the grounding line. Differences can be observed especially close to the subglacial water discharge locations. The average melt rates in box G (600 m by 600 m area with the center located at 99.6 W and 75.3 S [Figure 1]), close to the source of subglacial freshwater discharge R1, are 80.6, 148, 175, 292, and 389 m yr^{-1} for CTRL, Qsg, 2*Qsg, 10*Qsg, and 50*Qsg, respectively (Table S2). The averaged melt rates in box H (600 m by 600 m area with the center located at 99.5 W and 75.1 S [Figure 1]), close to the source of subglacial discharge R2, are smaller by ~50% compared to the melt rate in box G. However, they increase in a similar way for CTRL, Qsg, 2*Qsg, 10*Qsg, and 50*Qsg, confirming the importance of subglacial freshwater discharge. The enhancement of melt rates by subglacial discharge relative to the CTRL case is highlighted by the melt ratio (Figures 3f and S2). The ice shelf melt ratio is especially high along the path of meltwater plumes initiated at R1 and R2, with ratios up to 10 for the 10*Qsg experiment.

Figure 3. Spatial patterns of 10-day mean simulated basal melt rate under Pine Island ice shelf for the control (CTRL), Qsg, and 10*Qsg cases (a–c). Close-ups for the region close to the grounding line are additionally shown. (d) Same as (a) with a different color scale to indicate small-scale features. (e and f) Melt ratios of Qsg to CTRL and 10*Qsg to CTRL cases. Horizontal distributions of meltwater fraction along 27.4 kg m^{-3} (g–i) and 27.6 kg m^{-3} (j–l) on day 29 for the CTRL, Qsg, and 10*Qsg cases, respectively. We note that at the model boundary, the passive tracer representing glacial melt is able to exit the model domain. The ice front is indicated by the orange lines in the panels (g–l). Red arrows in (g) indicate the locations of sub-ice shelf channels. The pink dashed lines show the locations of vertical section E-F (g, j).

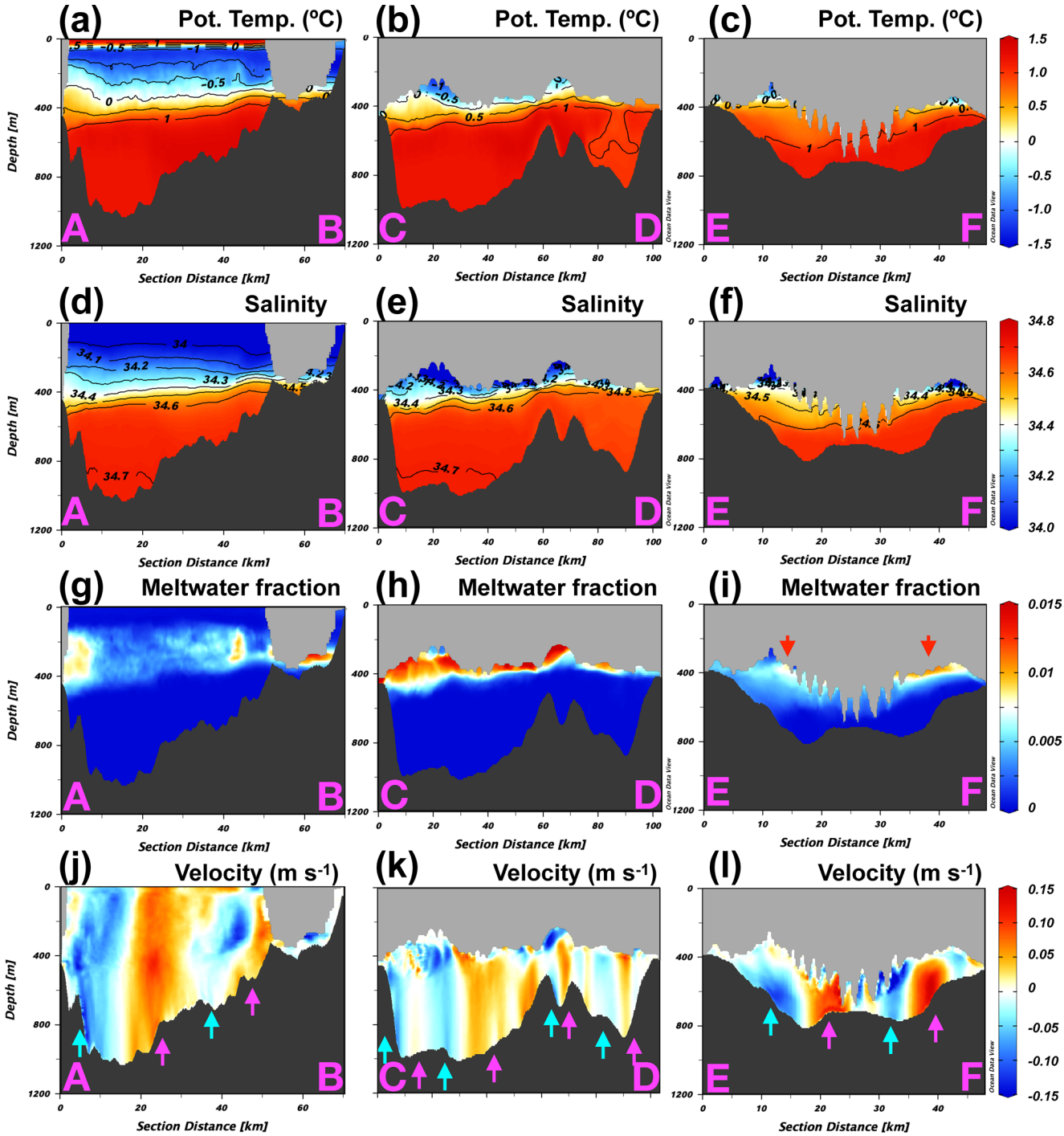

Figure 4. Ten-day average (day 20–29) potential temperature (a–c), salinity (d–f), glacial meltwater fraction (g–i), and east-southeastward ocean current (j–l) along the A-B (a, d, g, j), C-D (b, e, h, k), and E-F (c, f, i, l) sections, respectively, for control (see Figure 1 for location of sections). East-southeastward ocean current is selected as it aligns with the ice flow direction of Pine Island Glacier and is perpendicular to sections A-B, C-D, and E-F. Red arrows in (i) indicate the local maxima of the glacial meltwater fraction. Magenta (cyan) arrows in (j–l) show locations of ocean currents over the northward-shallowing (southward-shallowing) slopes.

Close to the grounding line, the higher ice shelf melt rates for experiments with subglacial freshwater discharge compared to CTRL can be primarily explained by the increase of ocean currents (Table S2). Currents in the uppermost grid cell below the ice shelf are 0.085 m s^{-1}, 0.15 m s^{-1}, 0.19 m s^{-1}, 0.31 m s^{-1}, and 0.46 m s^{-1} in box G for CTRL, Qsg, 2*Qsg, 10*Qsg, and 50*Qsg, respectively, while the thermal driving remains almost

unchanged (between 2.60 and 2.69, Figure S2). For the region further away from the grounding line, the higher melting area becomes larger and the magnitude of melting increases as subglacial freshwater flux increases. For example, the melt ratio between 10*Qsg and CTRL is 5–10 along the path of glacial meltwater plume (Figure 3f). This enhanced melt is primarily explained by the increase in uppermost ocean speed beneath the ice, but thermal driving also increases by a factor of 2 for locations with thin ice shelves away from the grounding line. The increased thermal driving is likely caused by the injection of subglacial freshwater discharge (~1°C warmer than the sea water freezing point at the grounding line), which forms more buoyant and warmer glacial meltwater plume filling spaces beneath ice (Figures 1, 3 and S2).

For CTRL, Qsg, and 2*Qsg, the impact of subglacial freshwater discharge on oceanographic properties is mostly limited to the region close to the grounding line (red arrows in Figure 2). Almost no changes are detected at the ice shelf front. For example, the strength of ocean circulation fluctuates for different sensitivity experiments without any noticeable trend (Figures 2 and S3). Vertical sections of glacial meltwater tracer remain almost identical (Figure 2). We are, however, able to observe different features for 10*Qsg and 50*Qsg experiments. Within 40 km from the grounding line, the 1°C isotherm deepens by ~40 and 80 m, respectively (Figure 2d). For the 50*Qsg case, the large amount of subglacial freshwater discharge forms a buoyant watermass, which ascends to the top of the ocean beneath the ice, filling all available spaces (Figure 2o). At the ice shelf front, this buoyant meltwater plume rises to the surface (Figure 2o). Strong glacial meltwater outflow can be found at the southern side of the PIIS front (Figure S3y). Oceanographic responses are large for 10*Qsg and 50*Qsg and it is likely that transient responses to new quasi-steady state are still ongoing at the end of the sensitivity experiments.

4. Discussion

Simulated PIIS melt rates increase from ~80 m yr^{-1} to ~150 m yr^{-1} over some area within 5–10 km from the grounding line (box G) when a realistic subglacial freshwater discharge (Qsg) is applied (Table S2). However, the overall effect of subglacial freshwater discharge is small; the average PIIS melt rate increases by just 5.7% for the Qsg case (Table S2). Only experiments 10*Qsg and 50*Qsg cause a significant change in the average basal melt.

Satellite-based estimates of PIIS melt rate show that melt rates have peak values of 200 m yr^{-1} at several locations within 5–10 km from the grounding line (Figure S4 in Shean et al., 2019). The integrated PIIS melt rate from satellite observations is ~90 Gt yr^{-1} for 2008–2015 (Shean et al., 2019). This means that the simulated total PIIS melt rate (~60 Gt yr^{-1} for the Qsg case) is smaller by ~50% and the total area with high melt (>150 m yr^{-1}) is reduced compared to observations (Figure S4). Such differences may arise from the ice shelf configuration used in this simulation with thicker ice close to the grounding zone. Thickening of PIIS, weakening of mCDW intrusions toward the grounding zone, and reduction in basal melting are suggested to have happened around 2014 (Christianson et al., 2016).

Large discharges, such as 10*Qsg and 50*Qsg, are not expected to happen in the coming decades. Subglacial lakes in the Pine Island basin have been observed to discharge ~0.1 – 0.15 Gt over periods of three weeks (Joughin et al., 2016; Milillo et al., 2017), roughly doubling the amount of subglacial discharge during these drainage events. Estimates of future rainfall and runoff over the grounded ice of Pine Island Glacier are also not expected to increase to large amounts over the coming century. Simulations of surface mass balance changes in the Amundsen Sea Sector by the end of the 21st century based on a regional atmospheric model forced with CMIP5 outputs show that the rainfall over the grounded part of Pine Island Glacier will increase from 0.1 to 0.3 Gt yr^{-1}, while the runoff over this same region will increase from 0 to 0.3 Gt yr^{-1} (Donat-Magnin et al., 2020).

Our simulations contrast with results from the Greenland Ice Sheet. In Greenland, subglacial discharge at the grounding line has been shown to drive fjord-scale circulation and to increase melting along the entire glacier terminus (Cai et al., 2017; Mankoff et al., 2016; Slater et al., 2018; Washam et al., 2020; Xu et al., 2012). The relatively minor effects of subglacial discharge on the average melt rate and circulation beneath PIIS especially for the CTRL, Qsg, and 2*Qsg cases contrast these results from Greenland. This contrast may be the results of differences in the amount of freshwater discharge at the grounding line, ice cavity geometry, and ocean conditions.

Our results are impacted by several limitations. High-resolution data, including the deep channels and other topographic features at the ice shelf base, are critical to capture detailed water pathways, sub-ice shelf circulation, and melt pattern (Adusumilli et al., 2020; Dutrieux et al., 2013; Nakayama et al., 2018; Shean et al., 2019; Wåhlin et al., 2021). Another limitation is the lack of feedback between ice melt from ocean heat flux and ice shelf draft elevation. This fixed draft prevents capturing feedback between basal melt, ice shelf base elevation and slopes or the formation and evolution of channels, known to impact basal melt (De Rydt & Gudmundsson, 2016; Favier et al., 2019; Milillo et al., 2019; Seroussi, Nakayama, et al., 2017; Shean et al., 2019). Higher melt rates might accelerate grounding line retreat and impact the stability of glaciers upstream, which is an important area for future study. We also note that our model simulation is only conducted for the PIIS austral summer conditions and pathways of glacial meltwater may be different for other seasons and other ice shelves (Zheng et al., 2021).

5. Conclusions

Satellite-based observations show that the PIIS melt rate is as high as ~200 m yr^{-1} close to the grounding line, but ocean simulations with realistic configuration have so far failed to reproduce such a high melt rate. Our experiment without subglacial freshwater discharge simulates an ice shelf melt rate of 58 Gt yr^{-1} with the highest values reaching ~80 m yr^{-1} close to the grounding line. When subglacial freshwater discharge originating from frictional heat and geothermal heat flux at the grounded ice base is added to the simulations, the average melt rate remains largely unchanged but freshwater discharge substantially enhances ice shelf melting close to the discharge location, successfully simulating high ice shelf melt rate, similar to remote-sensing estimates. Our results also suggest that the buoyant plume could rise to the surface at the ice shelf front only if very high amounts of freshwater discharge, about 50 times larger than those estimated for the current conditions were reached, making this unlikely to happen over the coming decades.

Data Availability Statement

The model code, input, and results are available at https://zenodo.org/record/5183196#.YRx2j9MzZ7I and https://ecco.jpl.nasa.gov/drive/files/ECCO2/High_res_PIG/PIG_only_200m. Each user must first register for an Earthdata account at https://urs.earthdata.nasa.gov/users/new in order to access these files in NASA Earthdata.

Acknowledgments
The authors thank Dimitris Menemenlis, Thiago Dias dos Santos, and Tyler Pelle for their useful comments and suggestions. The authors thank Lu An for her great support to make an efficient communication happening during this work. High-end computing resources were provided by the NASA Advanced Supercomputing (NAS) Division at the Ames Research Center. This work was supported by Grants-in-Aids for Scientific Research (19K23447, 21K13989) from the Ministry of Education, Culture, Sports, Science, and Technology in Japan. Helene Seroussi carried out research at the Jet Propulsion Laboratory, California Institute of Technology, under a contract with NASA, supported by grants from NASA Modeling, Analysis, and Prediction (MAP), Sea Level Change Science Team, and Cryospheric Science Programs. Insightful comments from the two anonymous reviewers were very helpful for improvement of the manuscript.

References

Adusumilli, S., Fricker, H. A., Medley, B., Padman, L., & Siegfried, M. R. (2020). Interannual variations in meltwater input to the Southern Ocean from Antarctic ice shelves. *Nature Geoscience*, *13*(9), 616–620. https://doi.org/10.1038/s41561-020-0616-z

Aschwanden, A., Bueler, E., Khroulev, C., & Blatter, H. (2012). An enthalpy formulation for glaciers and ice sheets. *Journal of Glaciology*, *58*(209), 441–457. https://doi.org/10.3189/2012JoG11J088

Biddle, L. C., Loose, B., & Heywood, K. J. (2019). Upper ocean distribution of glacial meltwater in the Amundsen Sea, Antarctica. *Journal of Geophysical Research: Oceans*, *124*(10), 6854–6870. https://doi.org/10.1029/2019jc015133

Cai, C., Rignot, E., Menemenlis, D., & Nakayama, Y. (2017). Observations and modeling of ocean-induced melt beneath Petermann Glacier Ice Shelf in northwestern Greenland. *Geophysical Research Letters*, *44*(16), 8396–8403. https://doi.org/10.1002/2017GL073711

Christianson, K., Bushuk, M., Dutrieux, P., Parizek, B. R., Joughin, I. R., Alley, R. B., et al. (2016). Sensitivity of pine island glacier to observed ocean forcing. *Geophysical Research Letters*, *43*(20), 10–817. https://doi.org/10.1002/2016gl070500

Cornford, S. L., Martin, D. F., Payne, A. J., Ng, E. G., Le Brocq, A. M., Gladstone, R. M., et al. (2015). Century-scale simulations of the response of the West Antarctic Ice Sheet to a warming climate. *The Cryosphere*, *9*, 1579–1600. https://doi.org/10.5194/tc-9-1579-2015

Cowton, T. R., Sole, A. J., Nienow, P. W., Slater, D. A., & Christoffersen, P. (2018). Linear response of east Greenland's tidewater glaciers to ocean/atmosphere warming. *Proceedings of the National Academy of Sciences*, *115*(31), 7907–7912. https://doi.org/10.1073/pnas.1801769115

Davis, P. E. D., Jenkins, A., Nicholls, K. W., Brennan, P. V., Abrahamsen, E. P., Heywood, K. J., et al. (2018). Variability in basal melting beneath Pine Island ice shelf on weekly to monthly timescales. *Journal of Geophysical Research: Oceans*, *123*, 8655–8669. https://doi.org/10.1029/2018JC014464

Depoorter, M., Bamber, J., Griggs, J., Lenaerts, J., Ligtenberg, S., van den Broeke, M., & Moholdt, G. (2013). Calving fluxes and basal melt rates of Antarctic ice shelves. *Nature*, *502*(7469), 89–92. https://doi.org/10.1038/nature12567

De Rydt, J., & Gudmundsson, G. (2016). Coupled ice shelf-ocean modeling and complex grounding line retreat from a seabed ridge. *Journal of Geophysical Research: Earth Surface*, *121*, 865–880. https://doi.org/10.1002/2015JF003791

Donat-Magnin, M., Jourdain, N. C., Gallée, H., Amory, C., Kittel, C., Fettweis, X., et al. (2020). Interannual variability of summer surface mass balance and surface melting in the Amundsen sector, West Antarctica. *The Cryosphere*, *14*(1), 229–249. https://doi.org/10.5194/tc-14-229-2020

Dutrieux, P., De Rydt, J., Jenkins, A., Holland, P. R., Ha, H. K., Lee, S. H., et al. (2014). Strong sensitivity of Pine island ice-shelf melting to climatic variability. *Science*, *343*(6167), 174–178. https://doi.org/10.1126/science.1244341

Dutrieux, P., Vaughan, D. G., Corr, H. F. J., Jenkins, A., Holland, P. R., Joughin, I., & Fleming, A. H. (2013). Pine Island Glacier ice shelf melt distributed at kilometre scales. *The Cryosphere*, *7*(5), 1543–1555. https://doi.org/10.5194/tc-7-1543-2013

Favier, L., Durand, G., Cornford, S. L., Gudmundsson, G. H., Gagliardini, O., Gillet-Chaulet, F., et al. (2014). Retreat of Pine Island Glacier controlled by marine ice-sheet instability. *Nature Climate Change*, *4*, 117–121. https://doi.org/10.1038/NCLIMATE2094

Favier, L., Jourdain, N. C., Jenkins, A., Merino, N., Durand, G., Gagliardini, O., et al. (2019). Assessment of sub-shelf melting parameterisations using the ocean–ice-sheet coupled model NEMO(v3.6)–Elmer/Ice(v8.3). *Geoscientific Model Development*, *12*, 2255–2283. https://doi.org/10.5194/gmd-12-2255-2019

Garabato, A. C. N., Forryan, A., Dutrieux, P., Brannigan, L., Biddle, L. C., Heywood, K. J., et al. (2017). Vigorous lateral export of the meltwater outflow from beneath an Antarctic ice shelf. *Nature*, *542*(7640), 219–222. https://doi.org/10.1038/nature20825

Hellmer, H., & Olbers, D. (1989). A two-dimensional model for the thermohaline circulation under an ice shelf. *Antarctic Science*, *1*(04), 325–336. https://doi.org/10.1017/s0954102089000490

Holland, D. M., & Jenkins, A. (1999). Modeling thermodynamic ice-ocean interactions at the base of an ice shelf. *Journal of Physical Oceanography*, *29*(8), 1787–1800. https://doi.org/10.1175/1520-0485(1999)029<1787:mtioia>2.0.co;2

Jacobs, S. S., & Giulivi, C. F. (2010). Large multidecadal salinity trends near the Pacific-Antarctic continental margin. *Journal of Climate*, *23*(17), 4508–4524. https://doi.org/10.1175/2010jcli3284.1

Jacobs, S. S., Jenkins, A., Giulivi, C. F., & Dutrieux, P. (2011). Stronger ocean circulation and increased melting under Pine Island Glacier ice shelf. *Nature Geoscience*, *4*(8), 519–523. https://doi.org/10.1038/ngeo1188

Jenkins, A. (1991). A one-dimensional model of ice shelf-ocean interaction. *Journal of Geophysical Research*, *96*(C11), 20671–20677. https://doi.org/10.1029/91jc01842

Jenkins, A., Dutrieux, P., Jacobs, S. S., McPhail, S. D., Perrett, J. R., Webb, A. T., & White, D. (2010). Observations beneath Pine Island Glacier in West Antarctica and implications for its retreat. *Nature Geoscience*, *3*(7), 468–472. https://doi.org/10.1038/ngeo890

Joughin, I., Shean, D. E., Smith, B. E., & Dutrieux, P. (2016). Grounding line variability and subglacial lake drainage on Pine Island Glacier, Antarctica. *Geophysical Research Letters*, *43*, 9093–9102. https://doi.org/10.1002/2016GL070259

Joughin, I., Smith, B. E., & Medley, B. (2014). Marine ice sheet collapse potentially under way for the Thwaites Glacier Basin, West Antarctica. *Science*, *344*(6185), 735–738. https://doi.org/10.1126/science.1249055

Joughin, I., Tulaczyk, S., Bamber, J. L., Blankenship, D., Holt, J. W., Scambos, T., & Vaughan, D. G. (2009). Basal conditions for Pine Island and Thwaites Glaciers, West Antarctica, determined using satellite and airborne data. *Journal of Glaciology*, *55*(190), 245–257. https://doi.org/10.3189/002214309788608705

Jourdain, N. C., Molinesa, J.-M., Le Sommera, J., Mathiot, P., Chanutc, J., de Lavergnee, C., & Madecd, G. (2019). Simulating of prescribing the influence of tides on the Amundsen Sea ice shelves. *Ocean Modelling*, *133*, 44–55. https://doi.org/10.1016/j.ocemod.2018.11.001

Kleiner, T., Rückamp, M., Bondzio, J. H., & Humbert, A. (2015). Enthalpy benchmark experiments for numerical ice sheet models. *The Cryosphere*, *9*(1), 217–228. https://doi.org/10.5194/tc-9-217-2015

Lenaerts, J. T., Van Den Broeke, M. R., Van De Berg, W. J., Van Meijgaard, E., & Kuipers Munneke, P. (2012). A new, high-resolution surface mass balance map of Antarctica (1979–2010) based on regional atmospheric climate modeling. *Geophysical Research Letters*, *39*(4). https://doi.org/10.1029/2011GL050713

Losch, M. (2008). Modeling ice shelf cavities in a z coordinate ocean general circulation model. *Journal of Geophysical Research*, *113*(C8). https://doi.org/10.1029/2007jc004368

Losch, M., Menemenlis, D., Heimbach, P., Campin, J.-M., & Hill, C. (2010). On the formulation of sea-ice models. Part 1: Effects of different solver implementations and parameterizations. *Ocean Modelling*, *33*, 129–144. https://doi.org/10.1016/j.ocemod.2009.12.008

Mankoff, K. D., Straneo, F., Cenedese, C., Das, S. B., Richards, C. G., & Singh, H. (2016). Structure and dynamics of a subglacial discharge plume in a Greenlandic fjord. *Journal of Geophysical Research: Oceans*, *121*, 8670–8688. https://doi.org/10.1002/2016JC011764

Milillo, P., Rignot, E., Mouginot, J., Scheuchl, B., Morlighem, M., Li, X., & Salzer, J. T. (2017). On the short-term grounding zone dynamics of Pine Island Glacier, West Antarctica, observed with Cosmo-SkyMed interferometric data. *Geophysical Research Letters*, *44*(20), 10–436. https://doi.org/10.1002/2017gl074320

Milillo, P., Rignot, E., Rizzoli, P., Scheuchl, B., Mouginot, J., Bueso-Bello, J., & Prats-Iraola, P. (2019). Heterogeneous retreat and ice melt of Thwaites Glacier, West Antarctica. *Science Advances*, *5*(1), eaau3433. https://doi.org/10.1126/sciadv.aau3433

Morlighem, M., Rignot, E., Binder, T., Blankenship, D., Drews, R., Eagles, G., et al. (2020). Deep glacial troughs and stabilizing ridges unveiled beneath the margins of the Antarctic ice sheet. *Nature Geoscience*, *13*(2), 132–137. https://doi.org/10.1038/s41561-019-0510-8

Morlighem, M., Rignot, E., Seroussi, H., Larour, E., Ben Dhia, H., & Aubry, D. (2010). Spatial patterns of basal drag inferred using control methods from a full-Stokes and simpler models for Pine Island Glacier, West Antarctica. *Geophysical Research Letters*, *37*(14). https://doi.org/10.1029/2010GL043853

Morlighem, M., Wood, M., Seroussi, H., Choi, Y., & Rignot, E. (2019). Modeling the response of northwest Greenland to enhanced ocean thermal forcing and subglacial discharge. *The Cryosphere*, *13*, 723–734. https://doi.org/10.5194/tc-13-723-2019

Mouginot, J., Rignot, E., & Scheuchl, B. (2014). Sustained increase in ice discharge from the Amundsen Sea Embayment, West Antarctica, from 1973 to 2013. *Geophysical Research Letters*, *41*(5), 1576–1584. https://doi.org/10.1002/2013GL059069

Nakayama, Y., Manucharayan, G., Kelin, P., Torres, H. G., Schodlok, M., Rignot, E., & Menemenlis, D. (2019). Pathway of circumpolar deep water into Pine Island and Thwaites ice shelf cavities and to their grounding lines. *Scientific Reports*, *9*, 16649.

Nakayama, Y., Menemenlis, D., Schodlok, M., & Rignot, E. (2017). Amundsen and Bellingshausen Seas simulation with optimized ocean, sea ice, and thermodynamic ice shelf model parameters. *Journal of Geophysical Research: Oceans*, *122*(8), 6180–6195. https://doi.org/10.1002/2016jc012538

Nakayama, Y., Menemenlis, D., Zhang, H., Schodlok, M., & Rignot, E. (2018). Origin of circumpolar deep water intruding onto the Amundsen and Bellingshausen Sea continental shelves. *Nature Communications*, *9*(1), 1–9. https://doi.org/10.1038/s41467-018-05813-1

Nakayama, Y., Schröder, M., & Hellmer, H. H. (2013). From circumpolar deep water to the glacial meltwater plume on the eastern Amundsen Shelf. *Deep-Sea Research I*, *77*, 50–62. https://doi.org/10.1016/j.dsr.2013.04.001

Nias, I. J., Cornford, S. L., & Payne, A. J. (2016). Contrasting the modelled sensitivity of the Amundsen Sea Embayment ice streams. *Journal of Glaciology*, *62*, 552–562. https://doi.org/10.1017/jog.2016.40

Paolo, F. S., Fricker, H. A., & Padman, L. (2015). Volume loss from Antarctic ice shelves is accelerating. *Science*, *348*(6232), 327–331. https://doi.org/10.1126/science.aaa0940

Pritchard, H. D., Ligtenberg, S. R. M., Fricker, H. A., Vaughan, D. G., Van den Broeke, M. R., & Padman, L. (2012). Antarctic ice-sheet loss driven by basal melting of ice shelves. *Nature*, *484*(7395), 502–505. https://doi.org/10.1038/nature10968

Rignot, E., Jacobs, S. S., Mouginot, J., & Scheuchl, B. (2013). Ice-shelf melting around Antarctica. *Science Express*, *341*, 226–270. https://doi.org/10.1126/science.1235798

Rignot, E., Mouginot, J., & Scheuchl, B. (2011). Ice flow of the Antarctic ice sheet. *Science*, *333*(6048), 1427–1430. https://doi.org/10.1126/science.1208336

Rignot, E., Mouginot, J., Scheuchl, B., van den Broeke, M., van Wessem, M. J., & Morlighem, M. (2019). Four decades of Antarctic ice sheet mass balance from 1979–2017. *Proceedings of the National Academy of Sciences*, *116*(4), 1095–1103. https://doi.org/10.1073/pnas.1812883116

Schodlok, M., Menemenlis, D., & Rignot, E. (2015). Ice shelf basal melt rates around Antarctica from simulations and observations. *Journal of Geophysical Research: Oceans*, *121*, 1085–1109. https://doi.org/10.1002/2015JC011117

Schwanghart, W., & Scherler, D. (2014). TopoToolbox 2—MATLAB-based software for topographic analysis and modeling in Earth surface sciences. *Earth Surface Dynamics*, *2*, 1–7. https://doi.org/10.5194/esurf-2-1-2014

Sciascia, R., Cenedese, C., Nicoli, D., Heimbach, P., & Straneo, F. (2014). Impact of periodic intermediary flows on submarine melting of a Greenland glacier. *Journal of Geophysical Research: Oceans*, *119*(10), 7078–7098. https://doi.org/10.1002/2014JC009953

Seroussi, H., Ivins, E. R., Wiens, D. A., & Bondzio, J. (2017). Influence of a West Antarctic mantle plume on ice sheet basal conditions. *Journal of Geophysical Research: Solid Earth*, *122*, 7127–7155. https://doi.org/10.1002/2017JB014423

Seroussi, H., Morlighem, M., Rignot, E., Khazendar, A., Larour, E., & Mouginot, J. (2013). Dependence of century-scale projections of the Greenland ice sheet on its thermal regime. *Journal of Glaciology*, *59*(218), 1024–1034. https://doi.org/10.3189/2013JoG13J054

Seroussi, H., Nakayama, Y., Larour, E., Menemenlis, D., Morlighem, M., Rignot, E., & Khazendar, A. (2017). Continued retreat of Thwaites Glacier, West Antarctica, controlled by bed topography and ocean circulation. *Geophysical Research Letters*, *44*(12), 6191–6199. https://doi.org/10.1002/2017GL072910

Shapiro, N. M., & Ritzwoller, M. H. (2004). Inferring surface heat flux distributions guided by a global seismic model: Particular application to Antarctica. *Earth and Planetary Science Letters*, *223*(1–2), 213–224. https://doi.org/10.1016/j.epsl.2004.04.011

Shean, D. E., Joughin, I. R., Dutrieux, P., Smith, B. E., & Berthier, E. (2019). Ice shelf basal melt rates from a high-resolution DEM record for Pine Island Glacier, Antarctica. *The Cryosphere*, *13*, 2633–2656. https://doi.org/10.5194/tc-13-2633-2019

Shepherd, A., Ivins, E., Geruo, A., Barletta, V., Bentley, M., Bettadpur, S., et al. (2012). A reconciled estimate of ice-sheet mass balance. *Science*, *338*(6111), 1183–1189. https://doi.org/10.1126/science.1228102

Shepherd, A., Ivins, E., Rignot, E., Smith, B., Van Den Broeke, M., Velicogna, I., et al. (2018). Mass balance of the Antarctic ice sheet from 1992 to 2017. *Nature*, *558*, 219–222. https://doi.org/10.1038/s41586-018-0179-y

Slater, D. A., Straneo, F., Das, S. B., Richards, C. G., Wagner, T. J. W., & Nienow, P. W. (2018). Localized plumes drive front-wide ocean melting of a Greenlandic tidewater glacier. *Geophysical Research Letters*, *45*, 12,350–12,358. https://doi.org/10.1029/2018GL080763

Straneo, F., Curry, R. G., Sutherland, D. A., Hamilton, G. S., Cenedese, C., Vage, K., & Stearns, L. A. (2011). Impact of fjord dynamics and glacial runoff on the circulation near Helheim Glacier. *Nature Geoscience*, *4*, 322–327. https://doi.org/10.1038/ngeo1109

Wåhlin, A. K., Graham, A. G. C., Hogan, K. A., Queste, B. Y., Boehme, L., Larter, R. D., et al. (2021). Pathways and modification of warm water flowing beneath Thwaites Ice Shelf, West Antarctica. *Science Advances*, *7*. https://doi.org/10.1126/sciadv.abd7254

Washam, P., Nicholls, K. W., Münchow, A., & Padman, L. (2020). Tidal modulation of buoyant flow and basal melt beneath Petermann Gletscher ice shelf, Greenland. *Journal of Geophysical Research: Oceans*, *125*(10). https://doi.org/10.1029/2020JC016427

Webber, B. G., Heywood, K. J., Stevens, D. P., Dutrieux, P., Abrahamsen, E. P., Jenkins, A., et al. (2017). Mechanisms driving variability in the ocean forcing of Pine Island Glacier. *Nature Communications*, *8*(1), 1–8. https://doi.org/10.1038/ncomms14507

Wei, W., Blankenship, D. D., Greenbaum, J. S., Gourmelen, N., Dow, C. F., Richter, T. G., et al. (2020). Getz ice shelf melt enhanced by freshwater discharge from beneath the West Antarctic ice sheet. *The Cryosphere*, *14*(4), 1399–1408. https://doi.org/10.5194/tc-14-1399-2020

Xu, Y., Rignot, E., Fenty, I., Menemenlis, D., & Flexas, M. M. (2013). Subaqueous melting of Store Glacier, west Greenland from three-dimensional, high-resolution numerical modeling and ocean observations. *Geophysical Research Letters*, *40*(17), 4648–4653. https://doi.org/10.1002/grl.50825

Xu, Y., Rignot, E., Menemenlis, D., & Koppes, M. (2012). Numerical experiments on subaqueous melting of Greenland tidewater glaciers in response to ocean warming and enhanced subglacial discharge. *Annals of Glaciology*, *53*(60), 229–234. https://doi.org/10.3189/2012aog60a139

Zheng, Y., Heywood, K. J., Webber, B. G., Stevens, D. P., Biddle, L. C., Boehme, L., & Loose, B. (2021). Winter seal-based observations reveal glacial meltwater surfacing in the southeastern Amundsen Sea. *Communications Earth & Environment*, *2*(1), 1–9. https://doi.org/10.1038/s43247-021-00111-z